Research Article Vol. 31, No. 3 / 30 Jan 2023 / *Optics Express* 4675

Optics EXPRESS

Kerr soliton frequency comb generation by tuning the coupling coefficient in coupled nonlinear microcavities

ZIHAO CHENG,[1,2] DONGMEI HUANG,[2,3,*] FENG LI,[1,2] CHAO LU,[1] AND P. K. A. WAI[1,2,4]

[1] *Photonics Research Institute, Department of Electronic and Information Engineering, The Hong Kong Polytechnic University, Hong Kong SAR, China*
[2] *The Hong Kong Polytechnic University Shenzhen Research Institute, Shenzhen 518057, China*
[3] *Photonics Research Institute, Department of Electrical Engineering, The Hong Kong Polytechnic University, Hong Kong SAR, China*
[4] *Department of Physics, Hong Kong Baptist University, Hong Kong SAR, China*
[*] *meihk.huang@polyu.edu.hk*

Abstract: Kerr soliton frequency comb generation in nonlinear microcavities with compact configurations are promising on-chip sources. Current Kerr comb generation by using a single microcavity with a tunable CW pump laser or high-power femtosecond pulse pump are difficult to be integrated on chip. In this paper, we propose an on-chip soliton comb generation scheme by tuning the coupling coefficient of two coupled microcavities instead of tuning the wavelength of the cw pump laser or using a pulsed pump laser in a single microcavity. The two microcavities are assumed to be identical. We showed by numerical simulation that Kerr comb generation is possible in both the blue and red detuned regions of the main microcavity in the coupled cavity system. We further found that the range and boundary of the soliton generation region of the couple microcavities depend on the coupling coefficient between the coupled cavities. To ensure that the modes being coupled have identical optical paths, we designed a Sagnac loop structure which couples the clockwise and counterclockwise modes in a single microcavity and demonstrated Kerr comb generation in both the blue and red detuned regions by tuning the coupling coefficient. The proposed Kerr comb generation scheme can be utilized for chip-scale integrated soliton comb sources, which will contribute to the development of on-chip applications.

1. Introduction

Microcavity based optical frequency combs are widely used in many fields including dual-comb spectroscopy [1], ultrafast optical ranging [2,3], comb LIDAR [4], atomic spectroscopy [5], coherent optical communications [6], photonic oscillators [7], optical coherence tomography [8], optical clock [9], microcavity astro-comb [10,11], etc. Compared with femtosecond laser combs, microcavity Kerr frequency combs with their compact structure, high power intensity, and low power consumption make them promise integrable comb sources for on-chip integration. Kerr frequency combs are generated by modulation instability and cascaded four-wave mixing through injection of the pump laser output into the microresonators with proper dispersion and nonlinearity management. A typical method for microcavity based soliton comb generation is to tune a continuous wave (cw) pump laser from the blue-detuned to the red-detuned frequency side [12,13]. In previous studies, it was found that the detuning of the pump cw laser must be within a certain range for the solitons to exist [14]. The soliton region corresponds to the bistable region of the stationary cw solution obtained from the LLE or Ikeda map [14,15]. Different techniques such as combined forward and backward cw pump laser [16], two-step "power kicking" by scanning the cw pump laser and decreasing the pump power with an acousto-optic modulator [17], and

#482228 https://doi.org/10.1364/OE.482228
Journal © 2023 Received 29 Nov 2022; revised 2 Jan 2023; accepted 3 Jan 2023; published 24 Jan 2023

slow frequency tuning of the pump laser in conjunction with phase or amplitude modulation [18] have been proposed to tune the pump laser wavelength into the soliton region for easy Kerr frequency comb generation. However, these methods all require a narrow linewidth tunable cw laser which is less stable, high cost and nearly impossible for chip-scale integration compared with a single wavelength laser. To avoid the use of a tunable laser with detuning, seeding the microresonator with a cw pump laser and a single shot pulse trigger has been proposed to generate Kerr combs, which also has the advantage of weaker thermal effect [19]. Although this method shows promising performance, the requirement of a high-power pulse laser is a hurdle for chip-scale integration. Another method to generate a Kerr frequency comb with a fixed single frequency pump laser is to thermally tune the resonance of the microcavity resonance [20]. The thermal tuning scheme is sensitive to the fluctuation of environment temperature and the tuning speed is low. Therefore, it remains a challenge to generate a stable Kerr comb without the use of a tunable laser.

In this paper, we proposed a novel method to achieve soliton comb generation without the use of tunable lasers by adjusting the coupling coefficient between two coupled nonlinear microcavities. In a coupled cavity structure, we found that the location of the soliton region is determined by the coupling coefficient between the two cavities and the soliton region can be continuously tuned to cover a wide range of detuning values. Thus, the soliton region can be tuned to reach the pump laser frequency without changing the pump laser wavelength, which makes on-chip soliton comb generation possible. More important, the soliton region can be tuned to the blue-detuned region such that soliton generation with a blue-detuned pump laser can be achieved by tuning the coupling coefficient. The blue-detuned region has higher thermal stability for cw-pumped microcavities [21]. We theoretically analyze the effect of the coupling coefficient on the soliton region by using the Ikeda map and numerically simulate the soliton frequency comb generation in coupled microcavities. Besides two coupled microcavities, we also propose a Sagnac loop like structure [22] with simple and easy fabrication to analyze the soliton region and numerically simulate soliton comb generation by tuning the coupling coefficient between the clockwise (CW) and counterclockwise (CCW) modes. We find that both the coupling coefficient of the coupled microcavities and Sagnac loop like structure can be tuned by adjusting the gap at the coupling region. The rest of the paper is organized as follows. Section 2 introduces the soliton comb generation in coupled nonlinear microcavities. We perform a stability analysis on the stationary solution to determine the soliton region in a coupled microcavities structure. In Section 3, we discuss the soliton region and soliton comb generation in a Sagnac loop coupling structure which coupled the like the CW and CCW modes. In Section 4, we investigate the effect of the coupling coefficient on the soliton region. Numerical simulations of soliton comb generation by tuning the coupling coefficient will be presented. Section 5 concludes the work.

2. Soliton comb generation in two coupled nonlinear microcavities and theoretical model

2.1. Theoretical model for two coupled microcavities

Figure 1 shows the schematic of two coupled nonlinear microcavities. The main cavity is coupled to a straight waveguide and an auxiliary cavity. The auxiliary cavity is coupled to another straight waveguide as well. For simplicity, we consider two identical microcavities which are made of the same material, have the same size, loss, nonlinearity, and dispersion coefficients. The power coupling coefficients θ between the straight waveguides and the microcavities are assumed to be the same. The power coupling coefficient between the two microcavities is θ_c. The main cavity is pumped by a cw laser with an amplitude of F. The optical fields inside the microcavities can be modeled by the modified Ikeda map [23] as

$$\frac{\partial E_1^{\mathrm{m}}(z,t)}{\partial z} = -i\Delta k_0 E_1^{\mathrm{m}} - \frac{\alpha}{2}E_1^{\mathrm{m}} - i\frac{\beta_2}{2}\frac{\partial^2 E_1^{\mathrm{m}}}{\partial t^2} + i\gamma|E_1^{\mathrm{m}}|^2 E_1^{\mathrm{m}}, \tag{1}$$

$$E_1^{\mathrm{n}}(0,t) = i\sqrt{\theta_{\mathrm{c}}}E_2^{\mathrm{m}}\left(\frac{L}{2},t\right) + \sqrt{1-\theta_{\mathrm{c}}}E_1^{\mathrm{m}}\left(\frac{L}{2},t\right), \tag{2}$$

$$\frac{\partial E_1^{\mathrm{n}}(z,t)}{\partial z} = -i\Delta k_0 E_1^{n} - \frac{\alpha}{2}E_1^{\mathrm{n}} - i\frac{\beta_2}{2}\frac{\partial^2 E_1^{\mathrm{n}}}{\partial t^2} + i\gamma|E_1^{\mathrm{n}}|^2 E_1^{\mathrm{n}}, \tag{3}$$

$$E_1^{\mathrm{m}}(0,t) = i\sqrt{\theta}F + \sqrt{1-\theta}E_1^{\mathrm{n}}\left(\frac{L}{2},t\right), \tag{4}$$

$$\frac{\partial E_2^{\mathrm{n}}(z,t)}{\partial z} = -i\Delta k_0 E_2^{\mathrm{n}} - \frac{\alpha}{2}E_2^{\mathrm{n}} - i\frac{\beta_2}{2}\frac{\partial^2 E_2^{\mathrm{n}}}{\partial t^2} + i\gamma|E_2^{\mathrm{n}}|^2 E_2^{\mathrm{n}}, \tag{5}$$

$$E_2^{\mathrm{m}}(0,t) = \sqrt{1-\theta}E_2^{\mathrm{n}}\left(\frac{L}{2},t\right), \tag{6}$$

$$\frac{\partial E_2^{\mathrm{m}}(z,t)}{\partial z} = -i\Delta k_0 E_2^{\mathrm{m}} - \frac{\alpha}{2}E_2^{\mathrm{m}} - i\frac{\beta_2}{2}\frac{\partial^2 E_2^{\mathrm{m}}}{\partial t^2} + i\gamma|E_2^{\mathrm{m}}|^2 E_2^{\mathrm{m}}, \tag{7}$$

$$E_2^{\mathrm{n}}(0,t) = i\sqrt{\theta_c}E_1^{\mathrm{m}}\left(\frac{L}{2},t\right) + \sqrt{1-\theta_c}E_2^{\mathrm{m}}\left(\frac{L}{2},t\right), \tag{8}$$

where z is the intracavity distance, E_1 and E_2 represent the optical fields inside the main cavity and the auxiliary cavity, respectively. $z=0$ denotes the coupling point between the two cavities. For both microcavities, the superscript m stands for the half of the cavity from the waveguide-microcavity coupling point to the microcavity-microcavity coupling point, i.e., z = 0, as shown in Fig. 1. The superscript n stands for the other half of the cavity from the microcavity-microcavity coupling point to the waveguide-microcavity coupling point. Δk_0 is the wave vector, and α is the intrinsic absorption coefficient per unit length of the microcavities. t is time, β_2 and γ are group velocity dispersion and nonlinear coefficients, respectively, of the two cavities. L is the roundtrip length of one cavity, and $|F|^2$ is the power of the cw pump laser.

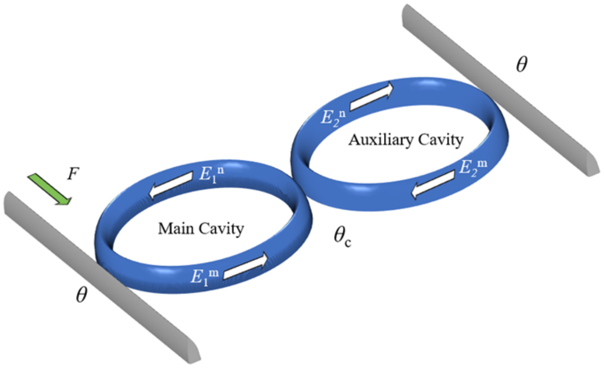

Fig. 1. Schematic of the coupled nonlinear microcavities.

2.2. *Stationary solutions and soliton region of the two coupled nonlinear microcavities*

We first consider continuous wave solutions and determine the soliton region of the two coupled nonlinear microcavities. We start from the auxiliary cavity. The cw solutions of Eqs. (5) and (7) are given by setting the temporal derivatives to zero. Thus, we have

$$E_2^{\mathrm{n}}\left(\frac{L}{2},t\right)=E_2^{\mathrm{n}}(0,t)\exp\left(-\frac{\alpha L}{4}-i\frac{\delta_0}{2}+i\gamma L_{\mathrm{eff}}|E_2^{\mathrm{n}}(0,t)|^2\right),\tag{9}$$

$$E_2^{\mathrm{m}}\left(\frac{L}{2},t\right)=E_2^{\mathrm{m}}(0,t)\exp\left(-\frac{\alpha L}{4}-i\frac{\delta_0}{2}+i\gamma L_{\mathrm{eff}}|E_2^{\mathrm{m}}(0,t)|^2\right),\tag{10}$$

where $\delta_0 = \Delta k_0 L$ is the detuning between the cw pump laser and the closest cold cavity resonance, $L_{\mathrm{eff}} = [1-\exp(-\alpha L/2)]/\alpha$ is the effective nonlinear length because of the intrinsic absorption. Substituting Eqs. (9) and (10) into Eqs. (6) and (8), we have

$$E_2^{\mathrm{m}}\left(\frac{L}{2},t\right)=E_2^{\mathrm{n}}(0,t)\sqrt{1-\theta}\exp\left(-\frac{\alpha L}{2}-i\delta_0+i\gamma M L_{\mathrm{eff}}|E_2^{\mathrm{n}}(0,t)|^2\right),\tag{11}$$

$$E_1^{\mathrm{m}}\left(\frac{L}{2},t\right)=\frac{i}{\sqrt{\theta_{\mathrm{c}}}}E_2^{\mathrm{n}}(0,t)\left[-1+\sqrt{1-\theta_{\mathrm{c}}}\sqrt{1-\theta}\exp\left(-\frac{\alpha L}{2}-i\delta_0+i\gamma M L_{\mathrm{eff}}|E_2^{\mathrm{n}}(0,t)|^2\right)\right],\tag{12}$$

where $M = 1 + (1-\theta)\exp(-\alpha L/2)$. By analyzing the cw solution for the auxiliary cavity, the optical field around the coupling point could be derived from $E_2^{\mathrm{m}}(0, t)$. We then determine the cw solution for the main ring by setting the temporal derivatives in Eqs. (1) and (3) to zero, we have

$$E_1^{\mathrm{m}}\left(\frac{L}{2},t\right)=E_1^{\mathrm{m}}(0,t)\exp\left(-\frac{\alpha L}{4}-i\frac{\delta_0}{2}+i\gamma L_{\mathrm{eff}}|E_1^{\mathrm{m}}(0,t)|^2\right),\tag{13}$$

$$E_1^{\mathrm{n}}\left(\frac{L}{2},t\right)=E_1^{\mathrm{n}}(0,t)\exp\left(-\frac{\alpha L}{4}-i\frac{\delta_0}{2}+i\gamma L_{\mathrm{eff}}|E_1^{\mathrm{n}}(0,t)|^2\right).\tag{14}$$

Substituting Eq. (13) into Eq. (12), we have

$$\begin{aligned}E_1^{\mathrm{m}}(0,t)=\frac{i}{\sqrt{\theta_{\mathrm{c}}}}E_2^{\mathrm{n}}(0,t)&\left[\sqrt{1-\theta_{\mathrm{c}}}\sqrt{1-\theta}\exp\left(-\frac{\alpha L}{2}-i\delta_0+i\gamma M L_{\mathrm{eff}}|E_2^{\mathrm{n}}(0,t)|^2\right)-1\right]\\&\times\exp\left(\frac{\alpha L}{4}+i\frac{\delta_0}{2}-i\gamma L_{\mathrm{eff}}|E_1^{\mathrm{m}}(0,t)|^2\right).\end{aligned}\tag{15}$$

Substituting Eqs. (11) and (12) into Eq. (2), we get

$$E_1^{\mathrm{n}}(0,t)=iE_2^{\mathrm{n}}(0,t)\left[\frac{\sqrt{1-\theta}}{\sqrt{\theta_{\mathrm{c}}}}\exp\left(-\frac{\alpha L}{2}-i\delta_0+i\gamma M L_{\mathrm{eff}}|E_2^{\mathrm{n}}(0,t)|^2\right)-\frac{\sqrt{1-\theta_{\mathrm{c}}}}{\sqrt{\theta_{\mathrm{c}}}}\right].\tag{16}$$

Solving Eq. (4) with Eqs. (14), (15), and (16), we obtain

$$\begin{aligned}\sqrt{\theta}F=E_2^{\mathrm{n}}(0,t)\frac{1}{\sqrt{\theta_{\mathrm{c}}}}&\left[\left(\sqrt{1-\theta_{\mathrm{c}}}\sqrt{1-\theta}N-1\right)\exp\left(\frac{\alpha L}{4}+i\frac{\delta_0}{2}-i\gamma L_{\mathrm{eff}}|E_1^{\mathrm{m}}(0,t)|^2\right)\right.\\&\left.-\sqrt{1-\theta}\left(\sqrt{1-\theta}N-\sqrt{1-\theta_{\mathrm{c}}}\right)\exp\left(-\frac{\alpha L}{4}-i\frac{\delta_0}{2}+i\gamma L_{\mathrm{eff}}|E_1^{\mathrm{n}}(0,t)|^2\right)\right],\end{aligned}\tag{17}$$

where $N = \exp(-\alpha L/2 - i\delta_0 + i\gamma M L_{\mathrm{eff}}\,|E_2^{\mathrm{n}}(0,t)|^2)$. Since the cw solutions of $|E_1^{\mathrm{m}}(0,t)|^2$, $|E_1^{\mathrm{n}}(0,t)|^2$ and N can be presented as functions of $|E_2^{\mathrm{n}}(0,t)|^2$, we can express the pump cw laser power $|F|^2$ as a function of $|E_2^{\mathrm{n}}(0,t)|^2$.

For soliton comb generation in the main cavity, previous studies have shown that the soliton region is related to the bistable steady-state condition between the pump laser power $|F|^2$ and the intracavity power $|E_1{}^{\mathrm{m}}(0,t)|^2$ [14,15]. In this coupled system, the relationship between $|F|^2$ and $|E_1{}^{\mathrm{m}}(0,t)|^2$ is indirect and are connected through $|E_2{}^{\mathrm{m}}(0,t)|^2$. From Eq. (15), we have

$$|E_1^{\mathrm{m}}(0,t)|^2 = \frac{1}{\theta_{\mathrm{c}}}|E_2^{\mathrm{n}}(0,t)|^2 \exp\left(\frac{\alpha L}{2}\right)\Big[(1-\theta_c)(1-\theta)\exp(-\alpha L)+1 -2\sqrt{1-\theta_{\mathrm{c}}}\sqrt{1-\theta}\exp\left(-\frac{\alpha L}{2}\right)\cos(-\delta_0+\gamma M L_{\mathrm{eff}}|E_2^{\mathrm{n}}(0,t)|^2)\Big], \tag{18}$$

where for a particular $|E_1{}^{\mathrm{m}}(0,t)|^2$, the corresponding $|E_2{}^{\mathrm{n}}(0,t)|^2$ can have multiple values depending on the parameters δ_0, θ, θ_{c}, and αL. If we include the multiple solutions here, the bistability behavior of the auxiliary cavity will create multi-value steady state solutions in the main cavity. In this parameter regime, the steady state solutions in the main cavity are multi-stable, rather than bistable. Thus, the multi-stability region is more complex, and we would not use this region to predict the soliton generation. If we approximate $\cos(-\delta_0 + \gamma M L_{\mathrm{eff}}|E_2{}^{\mathrm{n}}(0,t)|^2) \approx 1-0.5(-\delta_0+\gamma M L_{\mathrm{eff}}|E_2{}^{\mathrm{n}}(0,t)|^2)^2$, then for each $|E_1{}^{\mathrm{m}}(0,t)|^2$ value, Eq. (18) is a cubic polynomial equation of $|E_2{}^{\mathrm{n}}(0,t)|^2$. If we further only consider $\delta_0 < \sigma = (3\rho + 3/\rho - 6)^{1/2}$, where $\rho=[(1-\theta)(1-\theta_{\mathrm{c}})\exp(-\alpha L)]^{1/2}$, then each $|E_1{}^{\mathrm{m}}(0,t)|^2$ will have only one corresponding $|E_2{}^{\mathrm{n}}(0,t)|^2$ value and we will find the bistability region for steady state solutions in the main cavity. In the following Sections, we will assume δ_0 satisfies the inequality above. Using this assumption, we numerically obtain the multi-stable steady state conditions between $|E_1{}^{\mathrm{m}}(0,t)|^2$ and $|F|^2$. Figures 2(a) and 2(b) show two typical steady state solutions for $\delta_0 = -3\sigma$ and $-\sigma$, respectively. Here we assume $\theta_{\mathrm{c}} = \theta$. Similar to the single cavity, the numbers of solutions for $|E_1{}^{\mathrm{m}}(0,t)|^2$ under different $|F|^2$ depends on the value of δ_0. For $\delta_0 = -3\sigma$ in Fig. 2(a), there is always a unique solution. For $\delta_0 = -3\sigma$ in Fig. 2(b), there exists a range of pump power $|F(\delta_0)_-|^2 < |F|^2 < |F(\delta_0)_+|^2$, where $|F(\delta_0)_-|^2$ and $|F(\delta_0)_+|^2$ respectively denote the smaller and larger local extremum of the pump powers as shown in Fig. 2(b), in which there are three solutions $|E_1{}^{\mathrm{m}}(0,t)|^2$. Outside the interval $[|F(\delta_0)_-|^2, |F(\delta_0)_+|^2]$, there is only one solution. This is similar to the bistability behavior in dynamical systems with cubic nonlinearity, and previous studies suggest that the soliton comb generation is related to the bistability [14].

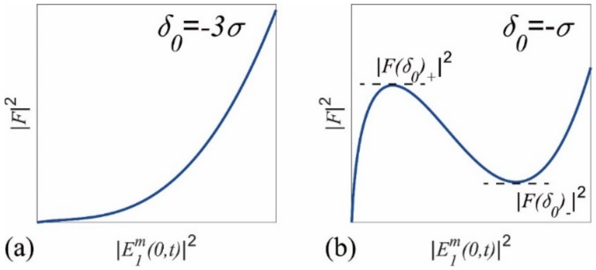

Fig. 2. The relationship between the number of steady state solutions in the main cavity and the pump power $|F|^2$. (a) For $\delta_0 = -3\sigma$, there is only one solution, and (b) for $\delta_0 = -\sigma$, there is a range of $|F|^2$ in which three solutions exist.

To illustrate how to obtain the bistable region, i.e., the possible soliton region, we scan the detuning value and calculate the corresponding $|F(\delta_0)_-|^2$ and $|F(\delta_0)_+|^2$ for a pair of coupled $\mathrm{Si_3N_4}$ microcavities as shown in Fig. 3(a). The parameters of the cavities are FSR = 226 GHz, $\Delta k_0 = -40.1$ /m, $\alpha = 19.1$ /m, $\beta_2 = -59$ ps^2/km, $\gamma = 1$ /W/m, and $\theta_{\mathrm{c}} = \theta = 0.0025$. The area shaded by dotted lines is the soliton region. The soliton region is similar to that of the single cavity discussed in [14], except that the soliton region of a single cavity exists only on the red-detuned side but the soliton region in coupled cavities can exist in both the red- and blue-detuned region. In coupled cavities, most of the bistability region near the cusp locates on the blue-detuned side. In the following, we focus on the blue-detuned bistability region in coupled cavities. We choose two different pumping parameters, one outside and the other inside the soliton region corresponding to points A and B, respectively, in Fig. 3(a), to investigate the formation of different stationary solutions. We numerically simulate Eqs. (1)–(8) to study the evolution of the optical fields inside the coupled cavities starting from a Gaussian pulse in the main cavity and white noise in the auxiliary cavity. The spectra of the initial fields in the cavities are shown with red dashed lines in Fig. 3. The pumping parameters outside (point A) and inside (point B) the soliton region are $\delta_0(\mathrm{A}) = -14.14\theta$, $|F|^2(\mathrm{A}) = 3$ W and $\delta_0(\mathrm{B}) = -11.78\theta$, $|F|^2(\mathrm{B}) = 3$ W, respectively. Figures 3(b) and 3(c) respectively show the temporal waveform and the spectrum in the main cavity after a simulation time of 60 ns for the pumping parameters at point A in Fig. 3(a). Both the temporal and spectral profiles of the initial Gaussian pulse evolve to the Turing pattern state which forms a Kerr comb characterized by isolated spectral lines with multiple FSR separations. Figures 3(d) and 3(e) respectively show the temporal waveform and spectrum in the auxiliary cavity after 60 ns. The temporal and spectral profiles are also the Turing pattern state with the same numbers of Turing rolls in the main cavity. Figures 3(f)–3(i) show the evolution of the initial Gaussian pulse with the pump inside the soliton region at point B. After a simulation time of 60 ns, single solitons are generated in both the main and auxiliary cavities as shown in Figs. 3(f) and 3(h). The peak powers of the solitons in the two cavities are nearly the same and the background cw power in the auxiliary cavity is higher. Figures 3(g) and 3(i) show that the spectra of the pulses in the two cavities are both hyperbolic secant in shape. The simulation results suggest that the conditions to generate soliton combs in coupled cavities are similar to that in a single cavity. A major difference is that the soliton region of the coupled cavities is shifted to the blue-detuned side for the coupling coefficient $\theta_\mathrm{c} = \theta$.

2.3. Soliton region with different coupling coefficients

In the results of Figs. 2 and 3, we assume $\theta_\mathrm{c} = \theta$. In this subsection, we consider the effect on the soliton region when the coupling coefficient between the two cavities θ_c varies. Figure 4(a) shows three different soliton regions for different coupling coefficients. We find that the soliton region blue shifts when the coupling coefficient increases. The soliton with the largest blue shift is at the cusp point of the soliton region. We define the detuning value and pump laser power at the cusp point as δ_p and $|F_\mathrm{p}|^2$, respectively. We investigate the evolutions of δ_p and $|F_\mathrm{p}|^2$ at the cusp point when the coupling coefficient increases from 0.5θ to 10θ. In Fig. 4(b), the detuning of cusp point continues to shift further into the blue-detuned region when θ_c increases. When θ_c increases from 0.5θ to 10θ, δ_p decreases from -9.1θ to -58.3θ. Figure 4(c) shows the corresponding change in the pump laser power at the cusp point. We note that $|F_\mathrm{p}|^2$ remains almost unchanged, decreasing only slightly from 1.515 to 1.495 W. Thus, $|\delta_\mathrm{p}|$ increases by ~540% while $|F_\mathrm{p}|^2$ decreases by only ~1.3% when θ_c increases from 0.5θ to 10θ. Thus, at the cusp point, the variation of θ_c mainly affects the detuning but has nearly no effect on the pump laser power.

In our previous work, we studied modulation instability (MI) in coupled microcavities with a blue-detuned pump laser [24]. The blue-detuned MI region is induced by the presence of a new figure-8 optical path which is created by the addition of the auxiliary cavity. Similarly, the blue-detuned soliton region is induced by the figure-8 optical path in the coupled microcavity system. As shown in Figs. 5(a) and 5(b), there are two optical paths inside the coupled microcavities that can couple light out to the straight waveguide which is coupled to the main cavity. Figure 5(a) shows a circular path going through the main cavity only and Fig. 5(b) shows a figure-8 path going through both the main and auxiliary cavities but in opposition direction. It should be noted that the coupling of the two cavities induces an additional π phase shift for the figure-8 optical path. Since the soliton region of a single cavity is located in the red-detuned region only, the

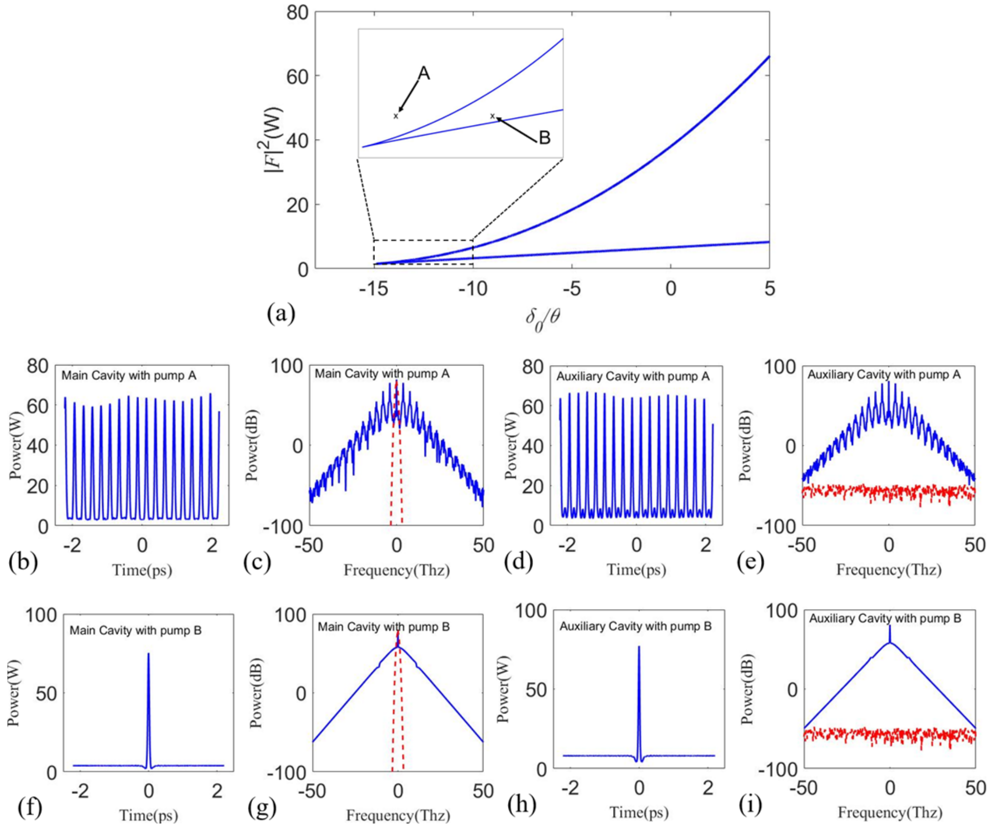

Fig. 3. (a) The soliton region (shaded by dotted lines) for coupled nonlinear cavities with $\theta_c = \theta$. The two blue solid curves correspond to $|F(\delta_0)_-|^2$ and $|F(\delta_0)_+|^2$. The (b) temporal and (c) spectral profiles of the Turing patterns generated in the main cavity with the pumping parameters at point A of Fig. 3(a). The corresponding (d) temporal and (e) spectral profiles in the auxiliary cavity. The (f) temporal and (g) spectral profiles of the soliton generation in the main cavity with pumping parameters at point B of Fig. 3(a). The corresponding (h) temporal and (i) spectral profiles in the auxiliary cavity. In the simulations, the initial condition in the main cavity is a Gaussian pulse and the initial condition in the auxiliary cavity is noise. The spectra of the initial fields in the cavities are presented with red dashed lines.

circular optical path in Fig. 5(a) does not cause the new blue-detuned soliton region. Thus, the blue-detuned soliton region is induced by the figure-8 optical path. The soliton region of the figure-8 optical path depends on the coupling coefficient between the two cavities θ_c. Figures 5(c) and 5(d) present the soliton regions of the figure-8 optical path for two extremum values of θ_c. In Fig. 5(c), when $\theta_c = 0$, the two microcavities are decoupled. The figure-8 path and the blue-detuned region it induced do not exist. The only soliton region remains is that of a single microcavity and it is located in the red-detuned region. In Fig. 5(d), when $\theta_c = 1$, all light inside the microcavities propagates in the figure-8 optical path and no light propagates in the main cavity only. The coupling induced π phase blue-shifts the soliton region of the figure-8 optical path to the very blue-detuned region and there is no red-detuned region in this case. Although no light propagates in the main cavity only, we still use the main cavity resonances to determine the bistability region for comparison. When the coupling coefficient θ_c is between 0 and 1, the soliton region of figure-8 optical path is between the two states shown in Fig. 5(c) and Fig. 5(d).

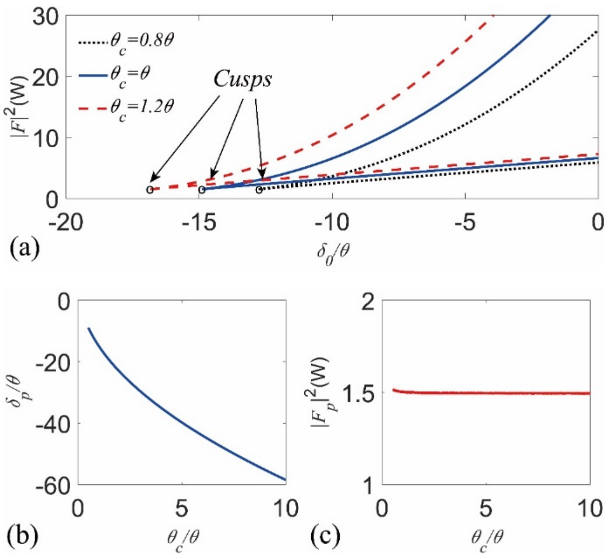

Fig. 4. (a) The soliton region of the coupled nonlinear microcavities with $\theta_\mathrm{c} = 0.8\theta$ (black dotted lines), θ (blue solid lines), and 1.2θ (red dashed lines). The (b) detuning and (c) power of the pump laser at the cusp point versus θ_c.

Figure 5(e) shows the soliton regions for $0 \leq \theta_c << 1$. When θ_c increases from 0, the power of the soliton region cusp $|F_\mathrm{p}|^2$ increases because of the higher total cavity loss induced by the auxiliary cavity. When θ_c increases from 0 to 5×10^{-4}, the soliton region shifts from the red-detuned to the blue-detuned side. Thus, the emergence of the blue-detuned soliton region is different from that of the blue-detuned MI region discussed in our previous work [24]. The blue-detuned MI region emerges directly at the blue detuned side when the coupling coefficient reaches the threshold, while the blue-detuned soliton region shifts from the red detuned side when the coupling coefficient increases. Although MI is the basis for soliton generation, their formation processes are different. The MI region can be deduced by applying the linear stability analysis on a specific mode, while soliton formation is a very nonlinear process involving thousands of modes. The soliton generation can start with any modes inside the soliton spectrum. Thus, the MI region and the soliton region are different. Figure 5(f) presents the soliton regions for $0 << \theta_c \leq 1$. When θ_c increases from 0.97 to 1, the soliton region keeps blue shifting. Overall, when the coupling coefficient θ_c increases from 0 to 1, the soliton region of the figure-8 optical path gradually blue-shifts from the state shown in Fig. 5(c) to that in Fig. 5(d). Figure 5(g) shows the evolution of the detuning at the cusp of the soliton region δ_p for different coupling coefficients θ_c. When θ_c increases from 0 to 1, δ_p continuously blue shifts from the red-detuned side to the very blue-detuned side.

Since the soliton region of the main-cavity-only optical path locates only in the red-detuned region, the blue-detuned soliton region is induced by the figure-8 optical path. While the pump cw laser is blue-detuned with respect to the resonance of the main cavity, it is red-detuned with respect to that of the figure-8 cavity. Figure 5(h) shows the resonances of the main cavity (top diagram), the resonances of the figure-8 cavity without a π phase shift (middle diagram), and the resonances of the figure-8 cavity with a π phase shift (lower diagram). The FSR of the figure-8 optical path is half of that of the main cavity and the coupling between the two microcavities induces a π phase blue shift to the resonances of the figure-8 optical path. From Fig. 5(h), the figure-8 optical path induced soliton region is blue-detuned with respect to the resonances of the main cavity but is red-detuned with respect to that of the figure-8 cavity.

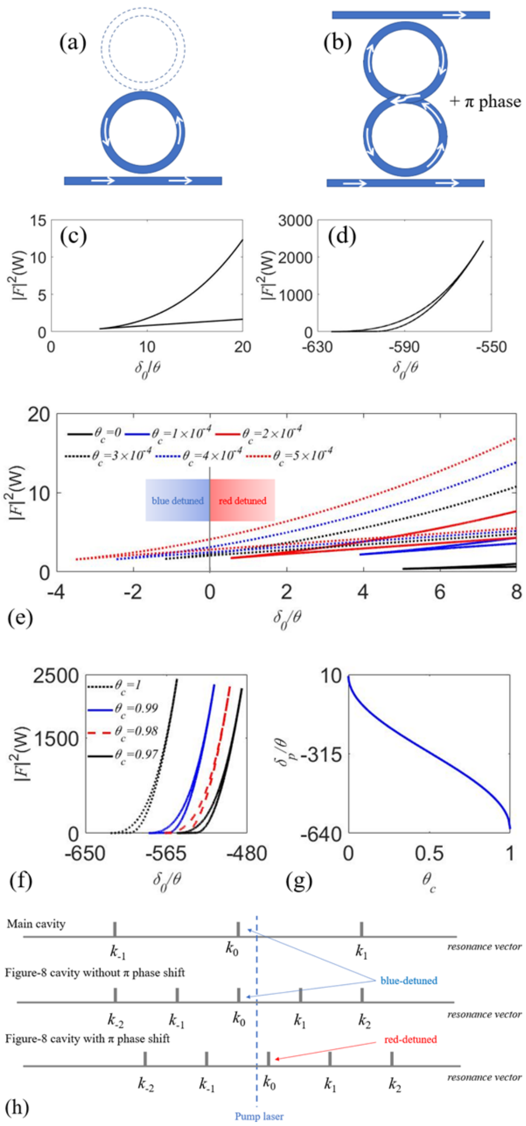

Fig. 5. (a) The optical path that propagates in the main microcavity only. (b) A figure-8 optical path induced by the addition of the auxiliary cavity. The coupling between the two microcavities introduced an additional π phase shift to the figure-8 optical path. The soliton regions of the (c) main cavity only optical path ($\theta_c = 0$) and (d) figure-8 optical path with $\theta_c = 1$. (e) The soliton region of the figure-8 optical path with $\theta_c = 0$ (black solid lines), 1×10^{-4} (blue solid lines), 2×10^{-4} (red solid lines), 3×10^{-4} (black dotted lines), 4×10^{-4} (blue dotted line), and 5×10^{-4} (red dotted lines). (f) The soliton region of the figure-8 optical path with $\theta_c = 0.97$ (black solid lines), 0.98 (red dashed lines), 0.99 (blue solid lines), and 1 (black dotted lines). (g) The evolution of the detuning at the cusp of the soliton region δ_p with coupling coefficient θ_c. (h) The cavity resonances of the main cavity (upper diagram), figure-8 cavity without π phase shift (middle diagram) and figure-8 cavity with π phase shift (lower diagram). The pump cw frequency is blue-detuned with respect to the resonance of the main cavity but red-detuned with respect to that of the figure-8 cavity.

3. Soliton comb generation in CW-CCW coupled microcavity

In practice, it is difficult to fabricate two microcavities with the same parameters. The requirement in fact is only that the light in the two microcavities have identical optical paths, which can be achieved if the two light waves are generated in the same microcavity. Various coupled mode structures including the coupling between different harmonics [25], polarization modes, different transverse modes, and CW-CCW modes [26,27] have been proposed to achieve that. The CW-CCW coupling is attractive for applications in turn-key soliton generation [28] and laser linewidth narrowing [29]. Since the coupling region between the CW and CCW modes is very small, the tuning of the intercavity or intermode coupling coefficient has higher tuning efficiency and better thermal stability when compared to that of the whole microcavity. In recent years, with the development of small size, low loss bend waveguides [30], similar structures have been experimentally demonstrated [31]. In the following, we investigate the soliton region and soliton comb generation in a Sagnac loop like structure by tuning the coupling coefficient of the CW-CCW modes.

3.1. Theoretical model

Figure 6 shows the schematic of a Sagnac loop like structure which can generate soliton comb by tuning the coupling between the CW and CCW modes. Equations (1)–(8) are not limited to two physically separated microcavities but can be used to describe the coupling of the CW and CCW modes in a single microcavity by adding cross phase modulation (XPM) between the coupled modes. We use the equations for the main cavity to describe the CCW mode, and the equations for the auxiliary cavity to describe the CW mode. If we use E_1 and E_2 to represent the optical fields of the CCW and CW modes, respectively, then Eqs. (2), (4), (6), and (8) do not need to be modified because they describe the coupling between the two modes. As Eqs. (1), (3), (5) and (7) describe light propagation inside the Sagnac loop like cavity, they should include the XPM terms as

$$\frac{\partial E_{1,2}(z,t)}{\partial z} = -i\Delta k_0 E_{1,2} - \frac{\alpha}{2}E_{1,2} - i\frac{\beta_2}{2}\frac{\partial^2 E_{1,2}}{\partial t^2} + i\gamma(|E_{1,2}|^2 + 2|E_{2,1}|^2)E_{1,2}. \tag{19}$$

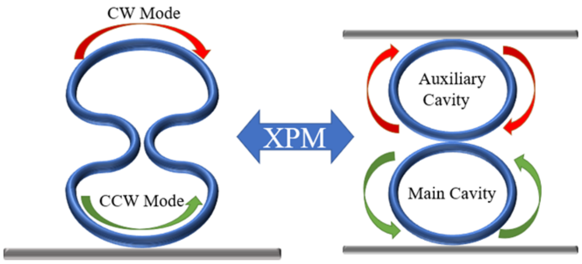

Fig. 6. The schematic of a Sagnac loop like microcavity with CW-CCW coupling.

3.2. Soliton generation in a CW-CCW coupled microcavity

With XPM, the stationary solution of the intracavity power of the CCW mode $|E_1|^2$ can no longer be simply presented as a function of $|E_2|^2$ like that in Eqs. (15) and (16). The determination of the soliton region for CW-CCW coupled cavities is therefore not straightforward. The effect of the additional XPM term is to increase the nonlinear phase change, so we expect the bistability region of a CW-CCW coupled microcavity would be similar to that of two physically separated microcavities. We use the soliton region of the coupled cavities without XPM as a reference to determine the soliton comb generation conditions in CW-CCW coupled cavities. Figure 7(a) presents the same soliton region as shown in Fig. 3(a), where the area shaded by dotted lines is the soliton region. We carried out numerical simulations of the optical field propagation in a CW-CCW microcavity starting from a Gaussian pulse with pumping conditions at point B and point C in Fig. 7(a). The cavity parameters and the pumping parameters at point B are the same as that in Fig. 3. The pumping parameters at point C are $\delta_0(\text{C}) = -13.55\theta$ and $|F|^2(\text{C}) = 0.6$ W. In physically separated coupled microcavities without XPM, the initial Gaussian pulse with pumping parameters at point B evolves to a single soliton state. However, Figs. 7(b) and 7(c) show that in the CW-CCW coupled microcavity, the initial Gaussian pulse in the CCW direction evolves to a chaotic state for the same pumping condition at point B. The corresponding temporal and spectral profiles in the CW direction shown in Figs. 7(d) and 7(e) are also in chaotic states. For the pumping parameters at point C, after propagation of 60 ns, the initial Gaussian pulse in the CCW direction evolves to a soliton molecule state as shown in Figs. 7(f) and 7(g). Figures 7(h) and 7(i) show the corresponding temporal and spectral profiles of the CW mode. The optical field of the CW mode is also in a soliton molecule-like state similar to the CCW mode. We observe

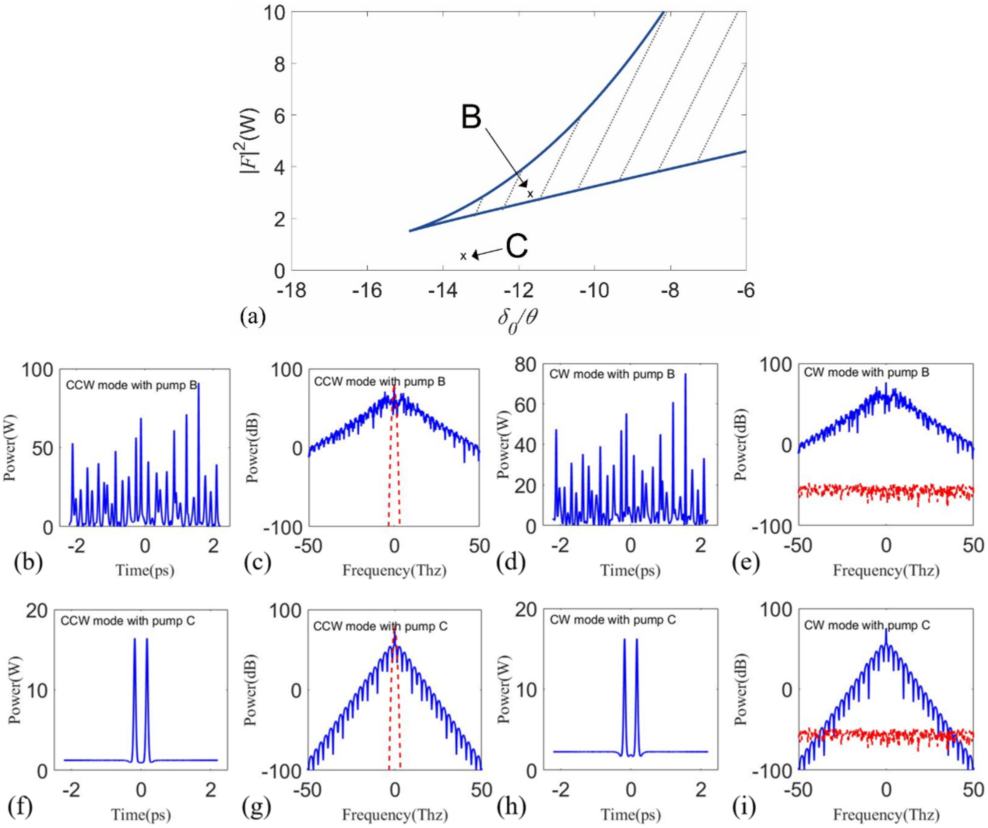

Fig. 7. (a) The soliton region of Fig. 3(a) repeated here as a reference for CW-CCW coupled microcavities. The (b) temporal and (c) spectral profiles of the Turing patterns generated in the CCW mode for the pumping parameters at point B in Fig. 7(a). The corresponding (d) temporal and (e) spectral profiles for the CW mode. The (f) temporal and (g) spectral profiles of the solitons generated in the CCW mode for the pumping parameters at point C of Fig. 7(a). The corresponding (h) temporal and (i) spectral profiles in the CW mode. In the simulations, the initial condition in the CCW mode is a Gaussian pulse and that in the CW mode is noise. The spectra of the initial fields in the cavities are presented with the red dashed lines.

that when XPM is included, the pump power required to generate a soliton frequency comb is lower that when XPM is not included. The reason is that XPM provides additional third order nonlinearity as shown in Eq. (18), thus more nonlinear phase is accumulated for the same power. The simulation results show that we can use the soliton region of physically separated coupled microcavities to guide the determination of the pumping conditions for the soliton generation in CW-CCW coupled cavities. In general, the choice of the detuning value should follow but the pump power should be lower than that in the soliton region determined in Section 2.

4. Soliton comb generation by tuning the coupling

4.1. *Soliton frequency comb generation in two coupled nonlinear microcavities by tuning the coupling coefficient*

We numerically simulated soliton comb generation by tuning the coupling coefficient of two coupled SiN microcavities. The simulation parameters are FSR = 226 GHz, $\Delta k_0 = -40.1$ /m, $\alpha = 19.1$ /m, $\beta_2 = -59$ ps^2/km, $\gamma = 1$ /W/m, $\theta = 0.0025$, and $|F|^2 = 3$ W. Figure 8 shows the simulation results of light propagation inside the main cavity and the auxiliary cavity. Figure 8(a) depicts the change in the coupling coefficient. In the first 8000 roundtrips (around 35 ns), θ_c increases linearly from 0 to θ and then stays constant at θ in the next 8000 roundtrips. Figures 8(b) and 8(c) show the evolution of the temporal and spectral profiles of the optical field in the main cavity. The intracavity optical field experiences MI and chaotic states before a single soliton emerges. Figures 8(d) and 8(e) respectively show the temporal and spectral profiles of the field in the main cavity at the final roundtrip (16000-th). Figures 8(f) and 8(g) show the corresponding temporal and spectral evolutions of the optical field in the auxiliary cavity. The field evolution in the auxiliary cavity is similar to that in the main cavity. MI grows at around the 6000-th roundtrip and after about another 2000 roundtrips, a single soliton emerges from a chaotic state. Figures 8(h) and 8(i) show the temporal and spectral profiles of the field in the auxiliary cavity at the final roundtrip, which are similar to that in the main cavity. The simulation results demonstrate that soliton combs can be generated by tuning the coupling coefficient in coupled microcavities. Compared with tuning the pump laser frequency, tuning the coupling coefficient has two major advantages. Firstly, this method avoids using tunable cw laser and makes it possible to achieve chip-scale integration for soliton comb generation. Secondly, the soliton generation region can be shifted to the blue-detuned region relative to the cold cavity resonance which makes the proposed soliton comb generation scheme thermally more stable.

4.2. *Soliton frequency comb generation in a CW-CCW coupled nonlinear microcavity by tuning the coupling*

We also numerically simulated the soliton comb generation by tuning the coupling coefficient in a CW-CCW coupled cavity. The simulation parameters are the same as that in Fig. 8 except $|F|^2 = 0.5$ W. Figure 9 shows the corresponding simulation results. The coupling coefficient linearly increases from 0 to θ in the first 8000 roundtrips and then keeps constant in the next 8000 roundtrips as shown in Fig. 9(a). Figures 9(b) and 9(c) show that the optical field in the CCW direction experiences an MI state and then a single soliton emerges from the Turing pattern. Figures 9(d) and 9(e) show the temporal and spectral profiles of the CCW mode at the 16000-th roundtrip. The corresponding optical field evolution in the CW direction is shown in Figs. 9(f) and 9(g). The optical field propagation of the CW mode is similar to that of the CCW mode. The temporal and spectral profiles of the single soliton generated in the CW direction at the 16000-th round trip are shown in Figs. 9(h) and 9(i). The simulation results demonstrate that the CW-CCW coupled microcavity provides a simple and effective solution to realize on-chip integrated soliton frequency comb sources.

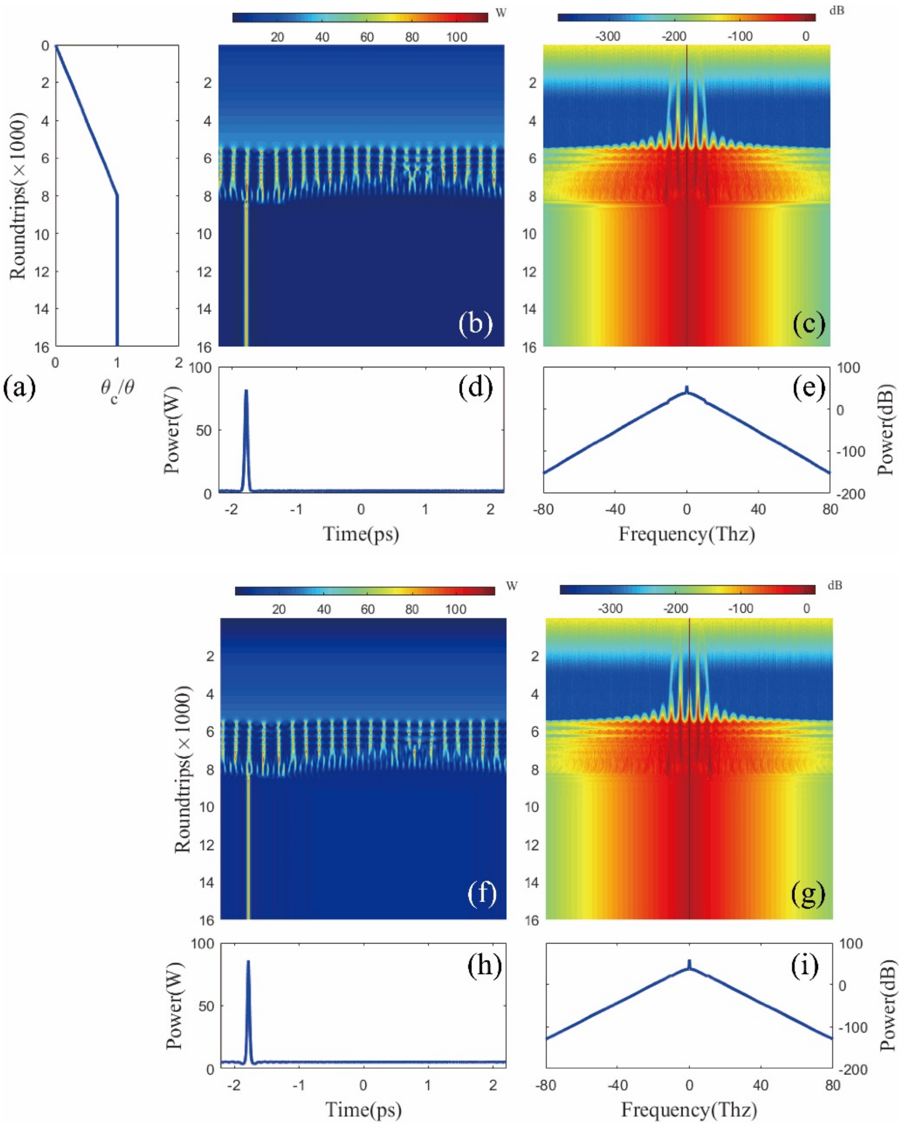

Fig. 8. (a) The change in the coupling coefficient in 16000 roundtrips. The (b) temporal and (c) spectral evolution of the intracavity optical field in the main cavity. The instantaneous (d) temporal and (e) spectral profiles of the optical field in the main cavity at the 16000-th roundtrip. The (f) temporal and (g) spectral evolution of the intracavity optical field in the auxiliary cavity. The instantaneous (h) temporal and (i) spectral profiles of the optical field in the auxiliary cavity at the 16000-th roundtrip.

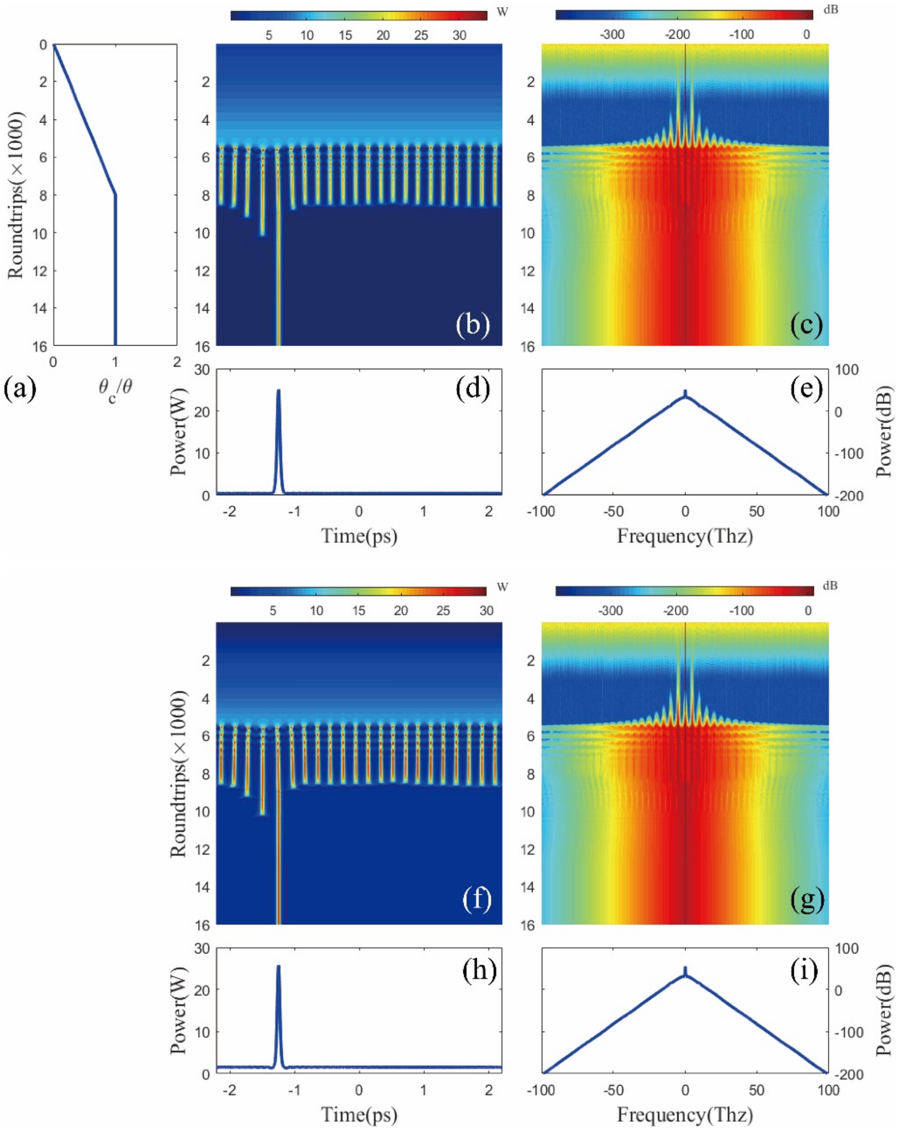

Fig. 9. (a) The change in the coupling coefficient in 16000 roundtrips. The (b) temporal and (c) spectral evolution of the intracavity optical field of the CCW mode. The instantaneous (d) temporal and (e) spectral profiles of the optical field of the CCW mode at the 16000-th roundtrip. The (f) temporal and (g) spectral evolution of the intracavity optical field of the CW mode. The instantaneous (h) temporal and (i) spectral profiles of the optical field of the CW mode at the 16000-th roundtrip.

5. Conclusion

In conclusion, we propose and demonstrate a novel soliton frequency comb generation scheme based on tuning the coupling coefficient in coupled nonlinear microcavities. We theoretically analyze the bistable steady state condition and soliton region in coupled microcavities by using the modified coupled Ikeda map. For simplicity, we assume the two microcavities are identical. Compared with a single microcavity, the soliton region can locate within the blue-detuned region relative to the cold cavity resonance. We also found that the location of the soliton region depends on the coupling coefficient between the two cavities. The soliton region blue shifts when the coupling coefficient increases. Therefore, we can tune the soliton region to cover the pump laser wavelength to achieve frequency comb generation instead of tuning the pump laser wavelength into the soliton region. We then numerically demonstrated single soliton frequency comb generation in coupled nonlinear microcavities by tuning the coupling coefficient between the two coupled microcavities. The coupling between the two microcavities can be tuned by various approaches. For micro-disk cavities, the coupling can be tuned by adjusting the gap between the microcavities [32]. For microring cavities, the coupling can be tuned by integrating a microheater at the coupling region [33]. The requirement of tuning range depends on the initial frequency separation between the frequency of the pump cw laser and the soliton region. It is easy to move the soliton region to cover the pump cw frequency by tuning the coupling with current microheater techniques [34]. There is no requirement on the tuning speed. To overcome the difficulties to fabricate two identical microcavities, we further proposed a Sagnac loop like structure to achieve CW-CCW coupling in a single microcavity. The Sagnac loop like single cavity including the XPM can also achieve soliton comb generation by tuning the coupling coefficient between the CW and CCW modes. The proposed novel soliton comb generation scheme avoids the use of tunable cw lasers and achieves chip-scale integration, which contributes to the applications of on-chip comb source.

Funding. National Key Research and Development Program of China (2019YFB1803904); National Natural Science Foundation of China (62105274); Basic and Applied Basic Research Foundation of Guangdong Province (2021A1515012544); Science, Technology and Innovation Commission of Shenzhen Municipality (JCYJ20210324133406018); University Grants Committee (PolyU152241/18E).

Disclosures. The authors declare no conflicts of interest.

Data availability. Data underlying the results presented in this paper are not publicly available at this time but may be obtained from the authors upon reasonable request.

References

1. M.-G. Suh, Q.-F. Yang, K. Y. Yang, X. Yi, and K. J. Vahala, "Microresonator soliton dual-comb spectroscopy," Science **354**(6312), 600–603 (2016).
2. P. Trocha, M. Karpov, D. Ganin, M. H. P. Pfeiffer, A. Kordts, S. Wolf, J. Krockenberger, P. Marin-Palomo, C. Weimann, S. Randel, W. Freude, T. J. Kippenberg, and C. Koos, "Ultrafast optical ranging using microresonator soliton frequency combs," Science **359**(6378), 887–891 (2018).
3. M.-G. Suh and K. J. Vahala, "Soliton microcomb range measurement," Science **359**(6378), 884–887 (2018).
4. N. Kuse and M. E. Fermann, "Frequency-modulated comb LIDAR," APL Photonics **4**(10), 106105 (2019).
5. L. Stern, J. R. Stone, S. Kang, D. C. Cole, M.-G. Suh, C. Fredrick, Z. Newman, K. Vahala, J. Kitching, S. A. Diddams, and S. B. Papp, "Direct Kerr frequency comb atomic spectroscopy and stabilization," Sci. Adv. **6**(9), eaax6230 (2020).
6. P. Marin-Palomo, J. N. Kemal, M. Karpov, A. Kordts, J. Pfeifle, M. H. P. Pfeiffer, P. Trocha, S. Wolf, V. Brasch, M. H. Anderson, R. Rosenberger, K. Vijayan, W. Freude, T. J. Kippenberg, and C. Koos, "Microresonator-based solitons for massively parallel coherent optical communications," Nature **546**(7657), 274–279 (2017).
7. W. Liang, D. Eliyahu, V. S. Ilchenko, A. A. Savchenkov, A. B. Matsko, D. Seidel, and L. Maleki, "High spectral purity Kerr frequency comb radio frequency photonic oscillator," Nat. Commun. **6**(1), 7957 (2015).
8. X. Ji, X. Yao, A. Klenner, Y. Gan, A. L. Gaeta, C. P. Hendon, and M. Lipson, "Chip-based frequency comb sources for optical coherence tomography," Opt. Express **27**(14), 19896–19905 (2019).
9. S. B. Papp, K. Beha, P. Del'Haye, F. Quinlan, H. Lee, K. J. Vahala, and S. A. Diddams, "Microresonator frequency comb optical clock," Optica **1**(1), 10–14 (2014).
10. E. Obrzud, M. Rainer, A. Harutyunyan, M. H. Anderson, J. Liu, M. Geiselmann, B. Chazelas, S. Kundermann, S. Lecomte, M. Cecconi, A. Ghedina, E. Molinari, F. Pepe, F. Wildi, F. Bouchy, T. J. Kippenberg, and T. Herr, "A microphotonic astrocomb," Nat. Photonics **13**(1), 31–35 (2019).
11. M.-G. Suh, X. Yi, Y.-H. Lai, S. Leifer, I. S. Grudinin, G. Vasisht, E. C. Martin, M. P. Fitzgerald, G. Doppmann, J. Wang, D. Mawet, S. B. Papp, S. A. Diddams, C. Beichman, and K. Vahala, "Searching for exoplanets using a microresonator astrocomb," Nat. Photonics **13**(1), 25–30 (2019).
12. T. Herr, V. Brasch, J. D. Jost, C. Y. Wang, N. M. Kondratiev, M. L. Gorodetsky, and T. J. Kippenberg, "Temporal solitons in optical microresonators," Nat. Photonics **8**(2), 145–152 (2014).
13. D. C. Cole, E. S. Lamb, P. Del'Haye, S. A. Diddams, and S. B. Papp, "Soliton crystals in Kerr resonators," Nat. Photonics **11**(10), 671–676 (2017).

14. C. Godey, I. V. Balakireva, A. Coillet, and Y. K. Chembo, “Stability analysis of the spatiotemporal Lugiato-Lefever model for Kerr optical frequency combs in the anomalous and normal dispersion regimes,” Phys. Rev. A **89**(6), 063814 (2014).
15. T. Hansson and S. Wabnitz, “Frequency comb generation beyond the Lugiato–Lefever equation: multi-stability and super cavity solitons,” J. Opt. Soc. Am. B **32**(7), 1259–1266 (2015).
16. H. Guo, M. Karpov, E. Lucas, A. Kordts, M. H. P. Pfeiffer, V. Brasch, G. Lihachev, V. E. Lobanov, M. L. Gorodetsky, and T. J. Kippenberg, “Universal dynamics and deterministic switching of dissipative Kerr solitons in optical microresonators,” Nat. Phys. **13**(1), 94–102 (2017).
17. X. Yi, Q.-F. Yang, K. Y. Yang, and K. Vahala, “Active capture and stabilization of temporal solitons in microresonators,” Opt. Lett. **41**(9), 2037–2040 (2016).
18. V. E. Lobanov, G. V. Lihachev, N. G. Pavlov, A. V. Cherenkov, T. J. Kippenberg, and M. L. Gorodetsky, “Harmonization of chaos into a soliton in Kerr frequency combs,” Opt. Express **24**(24), 27382–27394 (2016).
19. Z. Kang, F. Li, J. Yuan, K. Nakkeeran, J. Nathan Kutz, Q. Wu, C. Yu, and P. K. A. Wai, “Deterministic generation of single soliton Kerr frequency comb in microresonators by a single shot pulsed trigger,” Opt. Express **26**(14), 18563–18577 (2018).
20. Z. Lu, W. Wang, W. Zhang, S. T. Chu, B. E. Little, M. Liu, L. Wang, C.-L. Zou, C.-H. Dong, B. Zhao, and W. Zhao, “Deterministic generation and switching of dissipative Kerr soliton in a thermally controlled micro-resonator,” AIP Adv. **9**(2), 025314 (2019).
21. T. Carmon, L. Yang, and K. J. Vahala, “Dynamical thermal behavior and thermal self-stability of microcavities,” Opt. Express **12**(20), 4742–4750 (2004).
22. C. Vázquez, S. E. Vargas, and J. M. S. Sánchez, “Sagnac Loop in Ring Resonators for Tunable Optical Filters,” J. Lightwave Technol. **23**(8), 2555–2567 (2005).
23. I. K. E. D. A. Kensuke, “Multiple-valued stationary state and its instability of the transmitted light by a ring cavity system,” Opt. Commun. **30**(2), 257–261 (1979).
24. Z. Cheng, D. Huang, F. Li, C. Lu, and P. K. A. Wai, “Modulation instability generation with blue-detuned pump laser in coupled microcavities,” J. Opt. Soc. Am. B **39**(6), 1655–1665 (2022).
25. X. Xue, F. Leo, Y. Xuan, J. A. Jaramillo-Villegas, P.-H. Wang, D. E. Leaird, M. Erkintalo, M. Qi, and A. M. Weiner, “Second-harmonic-assisted four-wave mixing in chip-based microresonator frequency comb generation,” Light: Sci. Appl. **6**(4), e16253 (2016).
26. S. Fujii, A. Hori, T. Kato, R. Suzuki, Y. Okabe, W. Yoshiki, A.-C. Jinnai, and T. Tanabe, “Effect on Kerr comb generation in a clockwise and counter-clockwise mode coupled microcavity,” Opt. Express **25**(23), 28969–28982 (2017).
27. M. L. Gorodetsky, A. D. Pryamikov, and V. S. Ilchenko, “Rayleigh scattering in high-Q microspheres,” J. Opt. Soc. Am. B **17**(6), 1051–1057 (2000).
28. Boqiang Shen, Lin Chang, Junqiu Liu, Heming Wang, Qi-Fan Yang, Chao Xiang, Rui Ning Wang, Jijun He, Tianyi Liu, Weiqiang Xie, Joel Guo, David Kinghorn, Lue Wu, Qing-Xin Ji, Tobias J. Kippenberg, Kerry Vahala, and John E. Bowers, “Integrated turnkey soliton microcombs,” Nature **582**(7812), 365–369 (2020).
29. W. Jin, Q.-F. Yang, L. Chang, B. Shen, H. Wang, M. A. Leal, L. Wu, M. Gao, A. Feshali, M. Paniccia, K. J. Vahala, and J. E. Bowers, “Hertz-linewidth semiconductor lasers using CMOS-ready ultra-high-Q microresonators,” Nat. Photonics **15**(5), 346–353 (2021).
30. X. Ji, J. K. Jang, U. D. Dave, M. Corato-Zanarella, C. Joshi, A. L. Gaeta, and M. Lipson, “Exploiting Ultralow Loss Multimode Waveguides for Broadband Frequency Combs,” Laser Photonics Rev. **15**(1), 2000353 (2021).
31. M. Cherchi, S. Ylinen, M. Harjanne, M. Kapulainen, and T. Aalto, “Dramatic size reduction of waveguide bends on a micron-scale silicon photonic platform,” Opt. Express **21**(15), 17814–17823 (2013).
32. C. Wang, W. R. Sweeney, A. Douglas Stone, and L. Yang, “Coherent perfect absorption at an exceptional point,” Science **373**(6560), 1261–1265 (2021).
33. Y. Zhang, Q. Liu, C. Mei, D. Zeng, Q. Huang, and X. Zhang, “Proposal and demonstration of a controllable Q factor in directly coupled microring resonators for optical buffering applications,” Photonics Res. **9**(10), 2006–2015 (2021).
34. M. E. Castagna, R. Modica, and S. Cascino, *et al.*, “A high stability and uniformity W micro hot plate,” Sens. Actuators, A **279**, 617–623 (2018).